

Quantification of External Enthalpy Controlled Combustion at Unity Damköhler Number



Fabian Hampp and Rune Peter Lindstedt

Abstract The use of external enthalpy support (e.g. via heat recirculation) can enable combustion beyond normal flammability limits and lead to significantly reduced emissions and fuel consumption. The present work quantifies the impact of such support on the combustion of lean ($\Phi = 0.6$) turbulent premixed DME/air flames with a Damköhler number around unity. The flames were aerodynamically stabilised against thermally equilibrated hot combustion products (HCP) in a back-to-burnt opposed jet configuration featuring fractal grid generated multi-scale turbulence ($Re \simeq 18,400$ and $Re_t > 370$). The bulk strain ($a_b = 750 \text{ s}^{-1}$) was of the order of the extinction strain rate ($a_q = 600 \text{ s}^{-1}$) of the corresponding laminar opposed twin flame with the mean turbulent strain ($a_t = 3200 \text{ s}^{-1}$) significantly higher. The HCP temperature ($1600 \leq T_{HCP}(\text{K}) \leq 1800$) was varied from close to the extinction point ($T_q \simeq 1570 \text{ K}$) of the corresponding laminar twin flame to beyond the unstrained adiabatic flame temperature ($T_{ad} \simeq 1750 \text{ K}$). The flames were characterised using simultaneous Mie scattering, OH-PLIF and PIV measurements and subjected to a multi-fluid analysis (i.e. reactants and combustion products, as well as mixing, weakly reacting and strongly reacting fluids). The study quantifies the (i) evolution of fluid state probabilities and (ii) interface statistics, (iii) unconditional and (iv) conditional velocity statistics, (v) conditional strain along fluid interfaces and (vi) scalar fluxes as a function of the external enthalpy support.

F. Hampp · R. P. Lindstedt (✉)
Department of Mechanical Engineering, Imperial College, London SW7 2AZ, UK
e-mail: p.lindstedt@imperial.ac.uk

F. Hampp
e-mail: f.hampp11@imperial.ac.uk

Nomenclature

Roman Letters

a	Rate of strain [s^{-1}].
\bar{c}	Reaction progress variable [-].
c	Progress variable; Instantaneous conditioning variable [-].
$\bar{c}u$	Scalar Flux [$m s^{-1}$].
D	Burner nozzle diameter [m].
Da	Conventional Damköhler number [-].
Da_{ign}	Turbulent auto-ignition Damköhler number [-].
$d_{p,x}$	Al_2O_3 particle diameter x% [m].
e	Planar rate of strain tensor [s^{-1}].
H	Burner nozzle separation [m].
I	OH signal intensity [-].
I^{\ddagger}	Reference signal intensity [-].
Ka	Conventional Karlovitz number [-].
Ka_{ign}	Auto-ignition Karlovitz number [-].
$[k]$	Theoretical concentration of species k [$mol m^{-3}$].
L_{η}	Kolmogorov length scale [m].
L_I	Integral length scale of turbulence [m].
N	Total number of images [-].
\hat{n}	Unit vector of the iso-contour normal [-].
\dot{Q}	Heat release rate [$W m^{-3}$].
Re_t	Turbulent Reynolds number [-].
S_L	Laminar burning velocity [$m s^{-1}$].
\hat{s}	Unit vector of the streamline tangent [-].
T	Temperature [K].
T_{ad}	Adiabatic flame temperature [K].
T_{ign}	Auto-ignition temperature [K].
T_{HCP}	Lower nozzle hot combustion product temperature [K].
U	Flow velocity [$m s^{-1}$].
\bar{U}	Mean unconditional axial velocity [$m s^{-1}$].
\bar{U}_{\dots}	Mean conditional axial velocity [$m s^{-1}$].
u	Velocity component [$m s^{-1}$].
$\sqrt{u'^2}$	Unconditional axial velocity fluctuation [$m s^{-1}$].
$\sqrt{u'^2}_{\dots}$	Conditional axial velocity fluctuation [$m s^{-1}$].
u_{rms}	Root mean square velocity fluctuation [$m s^{-1}$].
\bar{U}_s	Slip velocity [$m s^{-1}$].
\bar{V}	Mean unconditional radial velocity [$m s^{-1}$].
\dot{V}	Lower nozzle volumetric flow rate [$m^3 s^{-1}$].
$\sqrt{v'^2}$	Unconditional radial velocity fluctuation [$m s^{-1}$].
$\sqrt{v'^2}_{\dots}$	Conditional radial velocity fluctuation [$m s^{-1}$].
X	Mole fraction [-].

x	Axial coordinate [m].
x_s	Distance from origin of first thermal alteration [m].
y	Radial coordinate [m].

Greek Letters

β	Fluid state material surface [-].
δ_f	Laminar fuel consumption layer thickness [m].
ε_r	Rate of dissipation within the reactants [m ² s ⁻³].
Λ	Threshold value [-].
λ_B	Batchelor scale [m].
λ_D	Mean scalar dissipation layer thickness [m].
λ_{MF}	Multi-fluid spatial resolution [m].
λ_{PIV}	PIV spatial resolution [m].
ν_r	Reactants kinematic viscosity [m ² s ⁻¹].
ω	Planar vorticity tensor [s ⁻¹].
Φ	Equivalence ratio [-].
τ_c	Chemical timescale [s].
τ_η	Kolmogorov timescale [s].
τ_{ign}	Auto-ignition delay time [s].
τ_I	Integral timescale of turbulence [s].
ξ	Blending fraction [% _{vol}].

Sub-/Superscripts

0	Alignment at the origin; initial value.
‡	Reference value.
<i>BTB</i>	Back-to-burnt configuration.
<i>b</i>	Bulk flow motion.
<i>d</i>	Total.
<i>FS</i>	Fluid state.
<i>HCP</i>	Hot combustion products.
<i>I</i>	Integral scale; turbulent.
<i>i, j</i>	Pixel index.
<i>k</i>	Velocity component.
<i>M</i>	Mixing fluid iso-contour.
<i>m</i>	Mixing fluid.
<i>n</i>	Instantaneous image; normal.
<i>NE</i>	Nozzle exit.
<i>p</i>	Product fluid.
<i>q</i>	Extinction conditions.

R	Reactant fluid iso-contour.
r	Reactant fluid.
SR	Strongly reacting fluid iso-contour.
s	Strongly reacting (flamelet) fluid.
T	Dependency on HCP temperature.
t	Tangential.
WR	Weakly reacting fluid iso-contour.
w	Weakly reacting fluid.

1 Introduction

Low Damköhler number combustion has the potential to reduce NO_x emissions through stable fuel lean operation [1]. However, thermal support is typically required to sustain chemical reactions [2] with common enthalpy sources including exhaust gas recirculation (EGR) [3] and reactant preheating via heat exchangers [4]. Raising the initial temperature (T_0) via preheating reduces the chemical timescale [5]. The strongly fuel-dependent auto-ignition delay time may become sufficiently short at high T_0 to influence the combustion behaviour [6]. Several combustion concepts utilise the exhaust gas enthalpy to stabilise fuel lean combustion. Examples include flameless oxidation in gas turbine engines [7] and low NO_x burners [8]. Blending of high temperature (internal) EGR yields a complex competition of advanced chain branching, possibly supported by the presence of residual intermediates, and quenching due to the diluents (e.g. CO_2 and H_2O) [9]. The DNS data of Minamoto et al. [10] have shown that the broadening and distribution of chemically active zones is not solely dependent on turbulence, but is strongly affected by the dilution level and mixture reactivity. At low equivalence ratios, comparatively low levels of turbulence have been found sufficient to disturb and broaden the reaction zone [11]. In a related study, Zhou et al. [12] have shown a significant broadening of the CH layer that experiences a deeper penetration of CH_2O and OH [11, 13] with increasing turbulence intensity. Accordingly, flamelet-based bimodal descriptions that assume a negligible probability of encountering chemically active states become problematic [10].

Canonical configurations, e.g. the Sandia–Sydney piloted jet flames [14, 15] and the opposed jet configuration [16, 17], are frequently used to advance the fundamental understanding of combustion processes. Mastorakos et al. [2] investigated the removal of conventional flame extinction limits for lean premixed CH_4 flames using a back-to-burnt (BTB) opposed jet geometry. No extinction was observed for a burnt gas temperature > 1550 K. An unstable region was detected in the range from 1450 to 1550 K with conventional extinction criteria valid for reduced temperatures. Goh [18] and Coriton et al. [19] extended the study by means of a wide range of Φ and increased turbulence levels. Related combustion regime transitions in lean premixed JP-10 (exotetrahydrodicyclopentadiene) flames were studied by Goh et al. [20] and compared to conventional twin flames approaching extinction [21]. Hampf et al. [22, 23] investigated burning mode transitions from close to the corrugated flamelet into

the distributed reaction zone regime by varying the stoichiometry of lean premixed dimethyl ether (DME) flames at a constant turbulent Reynolds number ($Re_t \simeq 380$). A constant burnt gas state was used. Coriton et al. [24] have shown that lean counter-flowing combustion products promote stable operation compared to stoichiometric flames or hot inert gas due to a delayed radical pool depletion. The promotion of chain branching by intermediates has also been observed under moderate or intense low oxygen dilution (MILD) conditions by Abtahizadeh et al. [25].

The current study investigates the impact of the counter-flowing hot combustion products (HCP) on turbulent DME/air flames at a constant $Re_t \simeq 395$ and a close to unity Damköhler number ($Da \simeq 1.1$). DME was selected as it is regarded as an attractive alternative fuel [26, 27] with a comparatively well-established combustion chemistry [28]. The conditions mark the approximate transition from thin to distributed reaction zones in a conventional regime diagram [22]. The investigated HCP temperature range of $1600 \leq T_{HCP}(\text{K}) \leq 1800$ covers conditions from close to the extinction point ($T_q \simeq 1570$ K) of the corresponding laminar twin flame to beyond the unstrained adiabatic flame temperature ($T_{ad} \simeq 1750$ K). The flames were studied using simultaneous Mie scattering, OH-PLIF and PIV. The study quantifies the impact of the thermal support on burning modes via the (i) evolution of the probability of encountering multiple fluid states (i.e. reactants, combustion products, mixing, weakly reacting and strongly reacting fluids) and (ii) interface statistics, (iii) unconditional and (iv) conditional velocity statistics, (v) conditional strain on fluid state interfaces and (vi) scalar fluxes.

2 Experimental Set-up

The twin flame variant of the current opposed jet burner was developed by Geyer et al. [16]. The current revised back-to-burnt (BTB) configuration, schematically depicted in Fig. 1, is identical to that used by Hampp et al. [22, 23, 30, 31] with multi-scale turbulence [17, 32, 33] generated via a cross fractal grid (CFG) [18, 32]. Operation in the BTB mode [2, 19, 20, 22, 23] enables the stabilisation under fuel lean conditions. The premixed DME/air mixture was injected through the upper nozzle (UN) and stabilised against hot combustion products emerging from the lower nozzle (LN) as described below. The nozzle separation was set to one nozzle diameter ($D = 30$ mm).

2.1 Upper Nozzle Flow Conditions

Premixed DME/air ($\Phi = 0.60$, $T_0 = 320$ K) was injected through the UN at a constant bulk velocity ($U_b = 11$ m s⁻¹). The CFG, offering a blockage ratio of 65% with a maximum to minimum bar width ratio of 4, was installed 50 mm upstream of the UN exit and provided well-developed multi-scale turbulence with $Re_t \simeq 395$. The turbulent (τ_l) and chemical (τ_c) timescales of the UN reactant flow were maintained

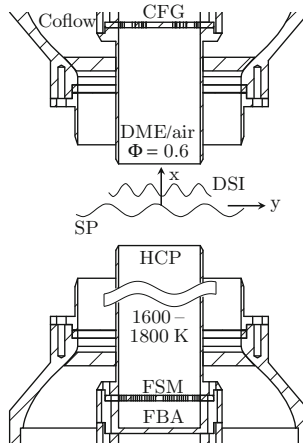


Fig. 1 Schematic of the experimental configuration. Unreacted premixed DME/air ($\Phi = 0.6$) is injected in the upper nozzle and stabilised by hot combustion products (HCP) from a stoichiometric $\text{H}_2/\text{CO}_2/\text{air}$ flame emerging the lower nozzle. CFG—cross fractal grid, DSI—density segregation iso-contour, SP—stagnation plane, FBA—flashback arrester, FSM—flame stabilisation mesh

constant and the investigated conditions occupy a nominally identical point in a conventional regime diagram with $Da \simeq 1.1$. The Re_t and τ_I were determined based on the integral length scale of turbulence ($L_I = 4.1$ mm) and the velocity fluctuations at the nozzle exit ($u_{rms} = 1.64$ m s $^{-1}$) measured using hot wire anemometry and particle image velocimetry (PIV), respectively. The calculated kinematic viscosity in the reactants was $\nu_r = 17.0 \times 10^{-6}$ m 2 s $^{-1}$. The Da number and τ_c , see Eq. 1, were estimated using a laminar burning velocity ($S_L = 0.21$ m s $^{-1}$) and a laminar flame thickness ($\delta_f = 0.22$ mm) [22] obtained from strained laminar opposed jet calculations ($a = 75$ s $^{-1}$) using the detailed chemistry of Park [28]. The flame thickness was based on the 5–95% fuel consumption thickness (i.e. inner thickness [34]).

$$\tau_I = \frac{L_I}{u_{rms}}, \quad \tau_c = \frac{\delta_f}{S_L}, \quad Re_t = \frac{L_I \cdot u_{rms}}{\nu_r}, \quad Da = \frac{\tau_I}{\tau_c} \quad (1)$$

The extinction strain of the corresponding laminar flame ($a_q = 600$ s $^{-1}$), the bulk ($a_b = 2 \cdot U_b/H = 750$ s $^{-1}$) and mean turbulent strain ($a_I = 3200$ s $^{-1}$) were determined by Hampf and Lindstedt [22].

2.2 Lower Nozzle Flow Conditions

The stabilising hot combustion products (HCP) were produced from highly diluted stoichiometric premixed H_2 flames anchored on a flame stabilisation mesh (FSM) located 100 mm upstream of the LN exit. The FSM was optimised to preclude any

Table 1 Lower nozzle conditions with X being the mole fractions (the missing percentile accounts for air), $[\text{OH}]_f^{\ddagger}$ the equilibrium OH concentration at the nozzle exit, $[\text{OH}]_q$ the peak OH concentration at the twin flame extinction point, \dot{V} the lower nozzle cold gas volumetric flow rate and U_{HCP} the HCP nozzle exit velocity.

Property	Unit	T_{HCP} [K]				
		1600	1650	1700	1750	1800
$X(\text{H}_2)$	–	0.218	0.230	0.238	0.244	0.249
$X(\text{CO}_2)$	–	0.263	0.225	0.197	0.175	0.159
$[\text{OH}]_f^{\ddagger} \times 10^{-3}$	mol m^{-3}	7.38	8.40	8.89	9.72	10.8
$[\text{OH}]_q \times 10^{-3}$	mol m^{-3}	30.9				
$\dot{V} \times 10^{-3}$	$\text{m}^3 \text{s}^{-1}$	3.11	3.11	3.10	3.08	3.06
U_{HCP}	m s^{-1}	22.7	23.4	24.1	24.6	25.1

flame instability and featured a blockage ratio of 62% with an aperture of 0.40 mm. A second finer mesh served as flashback arrestor (FBA). The HCP temperature at the nozzle exit was controlled from 1600 to 1800 K (peak-to-peak variation of 1%) by adjusting the CO_2 dilution rate from 15–25%_{vol} (prior combustion). The nozzle exit temperature was measured with a 50 μm R-type thermocouple. The lower limit corresponds approximately to the temperature at the twin flame extinction point ($T_q \simeq 1570$ K at $a_q = 600$ s^{-1}), and the upper limit exceeds the adiabatic flame temperature ($T_{ad} \simeq 1750$ K). The stagnation plane was positioned in the proximity of the burner centre by jet momentum matching with differences in HCP density compensated by modest adjustments of the cold gas bulk velocity as shown in Table 1.

2.3 Diagnostic Set-up

Simultaneous Mie scattering, PIV and hydroxyl planar laser-induced fluorescence (OH-PLIF) measurements were performed utilising the barium nitrate crystal technique of Kerl et al. [35] as detailed by Hampp et al. [22, 30]. The two overlaid light sheets (281.7 nm and 532 nm) exhibited a height of 1D and thicknesses <0.50 mm and <0.25 mm, respectively. The fluorescence signal was spectrally separated from the Mie scattering by a dichroic filter. Two interline-transfer CCD cameras (LaVision Imager Intense) were used with one connected to an intensified relay optics (LaVision IRO) unit to record the OH signal. The OH fluorescence was collected by a 105 mm ultraviolet lens ($f/2.8$) from LaVision and the Mie scattering with a Tokina AF 100 mm lens ($f/2.8$). Both lenses were equipped with bandpass filters featuring a transmissivity >85 % for the respective spectral range and an optical density >5 in order to block the laser lines. The PIV laser pulses were separated by 25 μs to minimise spurious vectors, and the OH-PLIF images were obtained from the

first laser pulse. Each nozzle was seeded separately using aluminium oxide powder ($d_{p,90} = 1.7 \mu\text{m}$). Cross-correlation PIV (LaVision Davis 8.1) was performed with decreasing interrogation regions size (128×128 to 48×48 with a 75% overlap). The final pass was conducted using a high accuracy mode and shape adaptation of the weighted windows to incorporate the local flow field acceleration [36]. The determined velocity field consisted of 115×88 vectors providing a spacing of 0.30 mm and spatial resolution of 0.60 mm. A comprehensive uncertainty analysis and the error associated with 3D effects were presented by Hampp et al. [22, 23].

For each condition, 3000 statistically independent realisations (minimum temporal separation of τ_I) were recorded. Image pre-processing (i.e. alignment, data reduction, noise reduction, shot-to-shot intensity fluctuations and white image correction) was performed as described by Hampp et al. [22, 30]. The well-defined conditions close to the upper and lower nozzle exits were used to obtain calibration signals in predefined interrogation windows [22].

3 Burnt Gas State and the Impact on Flame Parameters

The stabilisation of low Da flows against hot combustion products removes conventional extinction criteria with chemical reactions sustained by the thermal support [2]. By contrast, high Da self-sustained flames detach from the stagnation plane and decouple from the external enthalpy source influence [23]. The integrated heat release ($\int \dot{Q}$) of self-sustained flames correlates well with the thermochemical state (e.g. peak radical concentrations and peak temperature) and has been shown to be close to configuration (twin or BTB) independent [22]. The peak OH concentration at the twin flame extinction point ($[\text{OH}]_q = 30.9 \times 10^{-3} \text{ mol m}^{-3}$; see Table 1) can thus be used to approximately delineate self-sustained burning in the BTB configuration. The determined twin flame extinction point is independent of the HCP and is consequently constant in the current investigation. By contrast, the chemical activity of thermally supported burning with $\int \dot{Q}_{BTB} < \int \dot{Q}_q$ is influenced or governed by the HCP and dependent on the mixture composition and temperature of the external enthalpy source [9, 24, 25].

3.1 Burnt Gas State

The temperature of the HCP was controlled by means of CO_2 dilution prior combustion of the stoichiometric H_2 flames; see Sect. 2.2. The extended lower nozzle (100 mm) realised HCP in (close to) thermochemical equilibrium at the nozzle exit, which provided a well-defined experimental reference state [22]. In order to provide a reference point for comparisons with theoretical considerations, the latter can also be estimated using laminar flame calculations replicating the experimental conditions (i.e. mixture composition and residence time). The computations featured 660 locally

refined cells providing a resolution of $7 \mu\text{m}$ in the reaction zone. The measured and computed temperatures were matched using an overall heat loss of 7.2–8.9% via a radiation correction [37]. The estimated OH concentrations ($[\text{OH}]_T^\ddagger$) at the nozzle exit range from 7.38 to $10.8 \times 10^{-3} \text{ mol m}^{-3}$; see Table 1.

3.2 HCP Impact on Combustion Properties

The failure to establish self-sustained flames in the BTB opposed jet configuration results in turbulent mixing of the HCP with unreacted DME/air [23]. The blending of hot products with fresh reactants increases the initial temperature, reduces the auto-ignition delay times, alters burning properties (e.g. increased S_L and reduced δ_f) [9, 30] and thus eases ignition [38]. Under such conditions flamelet-like structures can coexist with pockets undergoing auto-ignition [39, 40]. Conventional definitions of the integral (τ_I), Kolmogorov (τ_η) and chemical (τ_c) timescales, associated with self-sustained burning, define the Da number (see Eq. 1) and the corresponding Karlovitz (Ka) number as shown in Eq. 2.

$$L_\eta = \left(\frac{v_r^3}{\varepsilon_r} \right)^{1/4}, \quad \tau_\eta = \sqrt{\frac{v_r}{\varepsilon_r}}, \quad Ka = \frac{\tau_c}{\tau_\eta} \quad (2)$$

The rate of dissipation (ε_r) in the reactants was obtained using the method of George and Hussein [41] for locally axisymmetric turbulence as described by Hampp and Lindstedt [22].

The potential influence of auto-ignition was estimated in terms of the associated delay times (τ_{ign}) as a function of the blending fraction (ξ) of reactants with HCP using shock tube calculations, see Fig. 2, where ξ is defined as nil in the reactants and unity in the HCP. With increasing T_{HCP} and ξ , the auto-ignition delay time decreases. The corresponding Damköhler and Karlovitz numbers based on the auto-ignition delay time (τ_{ign}) are defined below.

$$Da_{ign} = \frac{\tau_I}{\tau_{ign}}, \quad Ka_{ign} = \frac{\tau_{ign}}{\tau_\eta} \quad (3)$$

At a given initial temperature, Da_{ign} and Ka_{ign} provide a measure of the likelihood of the mixture being subject to auto-ignition in fluid pockets with mixing timescales corresponding to the large- and small-scale turbulent motion. The blending fraction required to cause an auto-ignition delay time similar to the integral timescale of turbulence ($\tau_{ign} = \tau_I \rightarrow Da_{ign} \sim 1$) is reduced from $\xi = 0.70$ to 0.55 as T_{HCP} is increased from 1600 and 1800 K. The data are summarised in Table 2.

Fig. 2 Shock tube calculations to evaluate the auto-ignition delay time (τ_{ign}) as function of blending fraction ξ and T_{HCP} . The horizontal dashed lines show the integral (τ_I) and Kolmogorov timescales (τ_η)

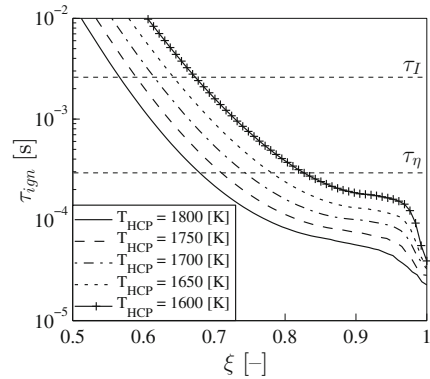


Table 2 Summary of turbulent and chemical parameters used to derive the turbulent Reynolds, Damköhler and Karlovitz numbers for DME/air at $\Phi = 0.6$ at a low strain rate ($a = 75 \text{ s}^{-1}$). The turbulence conditions were evaluated within the reactants. The auto-ignition delay times (τ_{ign}), Da_{ign} and Ka_{ign} were evaluated at the respective T_{HCP}

T_{HCP}	K	1800	1750	1700	1650	1600
Φ	–	0.60				
S_L	m s^{-1}	0.21				
δ_f	mm	0.46				
τ_c	ms	2.19				
τ_{ign}	μs	5.07	6.66	8.96	12.4	17.6
u_{rms}	m s^{-1}	1.63	1.67	1.65	1.60	1.64
L_I	mm	4.1	4.1	4.1	4.1	4.1
τ_I	ms	2.51	2.46	2.48	2.56	2.50
L_η	μm	75	72	73	72	73
τ_η	ms	0.33	0.31	0.31	0.30	0.31
a_q	s^{-1}	600				
ε_r	$\text{m}^2 \text{ s}^{-3}$	158	178	172	183	176
$\nu_r \times 10^6$	$\text{m}^2 \text{ s}^{-1}$	17.0				
Re_t	–	393	403	397	385	395
Da	–	1.15	1.12	1.13	1.17	1.14
Da_{ign}	–	495	369	277	206	142
Ka	–	6.67	7.09	6.96	7.19	7.05
Ka_{ign}	–	0.015	0.021	0.029	0.041	0.057

4 Multi-fluid Post-processing

Hampp and Lindstedt [22, 23] presented an extension to bimodal (i.e. reactants and products) statistical descriptions by incorporating chemically active fluid states such as mixing, weakly and strongly reacting. The methodology, briefly summarised below, was found particularly beneficial for low Da flows and was consequently adopted in the present study in order to delineate the impact of the external enthalpy source on the combustion process. The identified fluids states are defined as:

Reactants:	Fresh reactants emerging from the UN that have not undergone any thermal alteration (i.e. no oxidation or mixing processes). The reactants were detected via a PIV tracer particle-based density segregation technique, e.g. [33, 42, 43], that is capable of detecting multiple and fragmented splines.
Mixing fluid:	A fluid state that has been exposed to a thermal change prior the onset of OH producing chemical reactions (i.e. via mixing with HCP). The mixing fluid is detected by superposition of the Mie scattering and OH-PLIF images and identified as regions with low seeding density and no OH signal.
Strongly reacting fluid:	Regions with a high OH signal intensity caused by self-sustained (e.g. flamelet) burning (see Sect. 4.1). Conventional aerothermochemistry conditions and extinction criteria apply [19, 44].
Weakly reacting fluid:	A fluid state with modest levels of OH, e.g. ultra lean flames sustained by thermal support from an external enthalpy source and/or combustion products approaching equilibrium (see Sect. 4.1).
Hot combustion products:	The HCP emerge the LN in close to chemical equilibrium and provide a well-defined reference state with constant OH concentration and signal intensity for a given temperature; see Table 1.

4.1 OH Containing Fluid States

Chemically active fluid states were delineated based on the OH signal intensity using two thresholds. The first is based on experimental data, and the second is linked to well-established combustion theories [22] as outlined below. The methodology uses a linear relation [22, 46] between the OH concentration and fluorescence intensity that was found sufficient for the conditions of interest (uncertainty < 10%) to identify characteristic intensity bands [22, 30, 45]. The OH fluorescence signal intensity at the lower nozzle exit provides the well-defined reference state (I_T^{\ddagger}) that is used for calibration. The segregation of the HCP from chemically active fluid material that

originates the DME combustion was based on the maximum measured OH signal for an isothermal case (upper nozzle $\Phi = 0.0$) [22, 30]. The limiting threshold was determined to $\Lambda_p = \lceil I/I_T^\ddagger \rceil = 2.0$ for all T_{HCP} . The excess OH was attributed to the oxidation of residual reactants in the HCP by the fresh UN air. The resulting iso-contour can be related to the gas mixing layer interface of Coriton et al. [19].

Self-sustained (strongly reacting) flames detach from the stagnation plane and decouple from the HCP [23]. However, high rates of strain may suppress conventional burning and result in thermally supported (weakly reacting) burning that is dominated by the HCP. The thermochemical state at the twin flame extinction point (e.g. $[\text{OH}]_q$; see Table 1) arguably provides a natural segregation of self-sustained from supported burning [22]. The strongly reacting fluid (i.e. self-sustained burning) is therefore assumed to be present in regions where the OH signal intensity exceeds the corresponding non-dimensional extinction threshold defined by Eq. 4, i.e. $I > \Lambda_{q(T)} \cdot I_T^\ddagger$ with $\Lambda_{q(1600\text{ K})} = 4.2$, $\Lambda_{q(1650\text{ K})} = 3.7$, $\Lambda_{q(1700\text{ K})} = 3.5$, $\Lambda_{q(1750\text{ K})} = 3.2$ and $\Lambda_{q(1800\text{ K})} = 2.9$. The corresponding $[\text{OH}]_T^\ddagger$ and $[\text{OH}]_q$ are listed in Table 1.

$$\Lambda_{q(T)} = \frac{[\text{OH}]_q}{[\text{OH}]_T^\ddagger} = \frac{I_q}{I_T^\ddagger} \quad \forall T \quad (4)$$

The weakly reacting fluid follows as $\Lambda_p < I/I_T^\ddagger < \Lambda_{q(T)}$ and can stem from (i) ignition events, (ii) decaying OH concentration in combustion products or (iii) chemically active material that is diluted by the HCP.

4.2 Multi-fluid Fields and Spatial Resolution

The identification of the individual fluid states from the instantaneous Mie scattering and OH-PLIF images and subsequent superposition leads to quinary multi-fluid fields. An example is shown in Fig. 3 for a flame with $\Phi = 0.6$ and $T_{HCP} = 1700\text{ K}$. The spatial resolution and uncertainty analysis of the planar PIV and multi-fluid images as well as the laminar flame thickness for DME/air at $\Phi = 0.6$ were determined by Hampp et al. [22, 23] and are summarised in Table 3. The integral length scale of turbulence is resolved with $L_I/\lambda_{PIV} \simeq 7$ and $L_I/\lambda_{MF} \simeq 16$.

5 Results and Discussion

The multi-fluid probability, interface and conditional velocity statistics were aligned at the first thermal alteration iso-contour (i.e. $x_s = 0$ and detected via the density segregation technique; see Fig. 3) to eliminate modest variations of the stagnation plane location. The multi-fluid probabilities (Sects. 5.1 and 5.2) and unconditional and conditional velocity statistics in Sects. 5.3 and 5.4 (besides the nozzle exit velocity profiles) were conditioned on the theoretical stagnation point streamline (SPS),

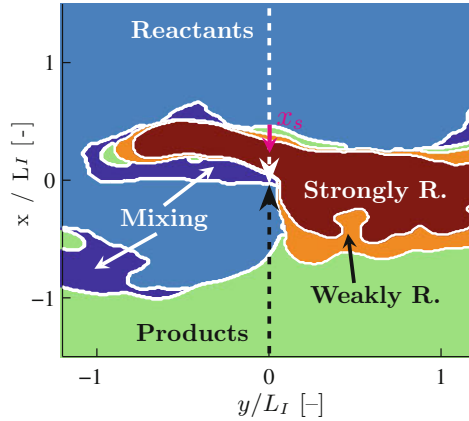


Fig. 3 Instantaneous quinary multi-fluid field for $T_{HCP} = 1700$ K with the vertical white/black arrows showing the theoretical stagnation point streamline (SPS). Interfaces are defined by the intersection of the SPS and material surfaces (white iso-contours). Reactants (light blue); Mixing (blue); Weakly reacting (orange); Strongly reacting (red); Products (green). The magenta arrow shows the x_s origin

Table 3 Physical and resolved length scales in μm , where λ_{PIV} and λ_{MF} are the PIV and multi-fluid resolutions, respectively. δ_f is the laminar flame thickness for a DME/air flame at $\Phi = 0.6$, λ_D is the mean scalar dissipation layer thickness [47] and λ_B the Batchelor scale [48]

Scales	Reactants	HCP
λ_{PIV}	598	
λ_{MF}	250	
δ_f	440	N.A.
λ_D	621 ± 18	N.A.
λ_B	86 ± 15	~ 370

i.e. $y = 0$ in Fig. 3. The strain analysis in Sect. 5.5 was condition on $y = 0 \pm 1/2 L_I$ to include the radial movement of the stagnation point [32].

5.1 Multi-fluid Statistics

The reactant fluid, aligned at $x_s = 0$, inherently drops from unity to nil (see Fig. 4 top left) yet recurs independent of T_{HCP} at $x_s > 0$ with a peak probability $\sim 5\%$ due to turbulent transport [22]. The influence of the HCP enthalpy becomes apparent in the mixing fluid probability as shown in the top right of Fig. 4. The probability is reduced away from the origin due to the earlier onset of OH producing chemical reactions with increasing enthalpy support. For $T_{HCP} > T_{ad}$, a reduction in the mixing fluid peak

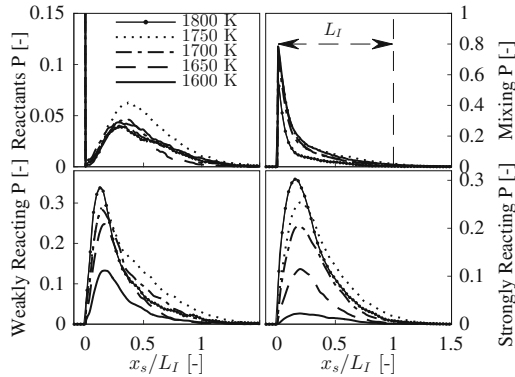


Fig. 4 Multi-fluid probability (P) for DME cases at $\Phi = 0.6$ with $T_{HCP} = 1600\text{--}1800$ K: Top left: Reactant fluid; Right: Mixing fluid; Bottom left: Weakly reacting fluid; Right: Strongly reacting (flamelet-like) fluid probability. The markers are drawn for identification purposes and do not represent the actual resolution

probability from 75 to 53 % is observed at $x_s = 0$ as OH producing chemical reactions are induced within a length scale below the multi-fluid resolution of $\simeq 250 \mu\text{m}$. The threefold increase of $Da_{ign} (= \tau_I / \tau_{ign}) = 140\text{--}500$ for $T_{HCP} = 1600\text{--}1800$ K results in a pronounced augmentation of the weakly reacting fluid peak probability from 13 to 35% as depicted in bottom left of Fig. 4. The strongly reacting fluid probability increases from 2% for $T_{HCP} = 1600$ K to approximately 30% for $T_{HCP} = 1800$ K. The combustion products make the balance for the missing percentiles. The spatial extent of all fluid probabilities is limited to approximately one integral length scale of turbulence (L_I) for all investigated conditions.

5.2 Multi-fluid Flow Structure

The interfaces encountered by traversing along the SPS through the quinary multi-fluid fields (see Fig. 5) are evaluated for three conditions: (i) the streamline tangent (\hat{s}) is approximately aligned with the iso-contour normal (\hat{n}) so that $\hat{s} \cdot \hat{n} > 0.05$, (ii) flow into the opposite direction with $\hat{s} \cdot \hat{n} < -0.05$ and (iii) tangential flow with $|\hat{s} \cdot \hat{n}| < 0.05$ (i.e. $72\text{--}108^\circ$), where \hat{s} and \hat{n} are defined positive in flow direction and from reactants to products, respectively. A schematic illustrating the three flow scenarios is shown in Fig. 5a with an example depicted in Fig. 5b. The diagrams in Fig. 6 show major flow paths (i.e. $>5\%$) for the $T_{HCP} = 1600, 1700$ and 1800 K cases. Reduced values of T_{HCP} result in a flow structure that highlights the need for extensive HCP blending to cause reaction onset and to sustain the chemical activity, i.e. primary fluxes through the mixing and weakly reacting fluid. The latter fluid state is predominately formed via fluxes from the HCP fluid due to smooth OH gradients [22] and longer auto-ignition delay times (see Fig. 2). By contrast, a high temperature burnt gas state promotes an earlier onset of OH producing chemical reactions and realises fluxes from the reactant fluid directly into strongly reacting

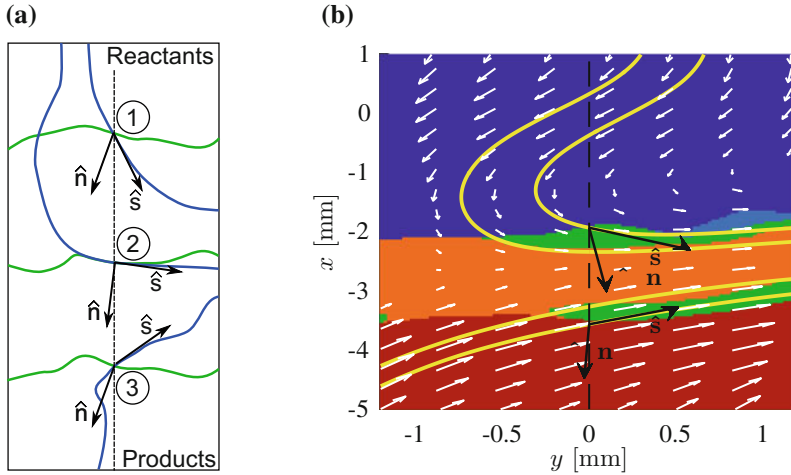


Fig. 5 **a** Schematic illustrating the three defined flow scenarios where blue lines represent streamlines and green lines iso-contours. The streamline tangent \hat{s} and the iso-contour normal \hat{n} are defined positive in flow direction and from reactants to products: (1) $\hat{s} \cdot \hat{n} > 0.05$, (2) $|\hat{s} \cdot \hat{n}| < 0.05$ (i.e. 72–108°) and (3) $\hat{s} \cdot \hat{n} < -0.05$. **b** Multi-fluid image at $T_{HCP} = 1800$ K with streamlines (yellow) and PIV vectors overlaid: reactants (blue), mixing, (light blue), weakly (green), strongly reacting (orange), products (red). The vertical dashed line shows the theoretical SPS and the arrows the unit vectors of the iso-contour normal (\hat{n}) and streamline tangent (\hat{s})

regions (e.g. a flamelet structure). However, the complex interaction of flame propagation, short auto-ignition delay times and high rates of strain cause fluxes from the reactants into all fluid states. The fluxes into the strongly reacting fluid via the weakly reacting and product fluid can be attributed to contact burning or small blending fractions. The weakly reacting fluid is still primarily formed via adjacent HCP layers indicating the strong need for thermal support for this fluid state.

5.3 Unconditional Velocity Statistics

The present work seeks to isolate the impact of the HCP temperature. The CO_2 concentration in the HCP stream was therefore the only parameter varied. This results in flow deviations/instabilities at the end points of $T_{HCP} = 1600$ and 1800 K, i.e. mean radial HCP velocities > 1 m/s at the theoretical stagnation point streamline and increased axial velocity fluctuations. Consequently, the following analysis focuses on the intermediate cases with $T_{HCP} = 1650, 1700$ and 1750 K. The HCP conditions can be optimised for a wider temperature range at the expense of additional changes in experimental parameters. The nozzle exit flow directions of the reactants and HCP are defined as negative and positive, respectively; see Fig. 1.

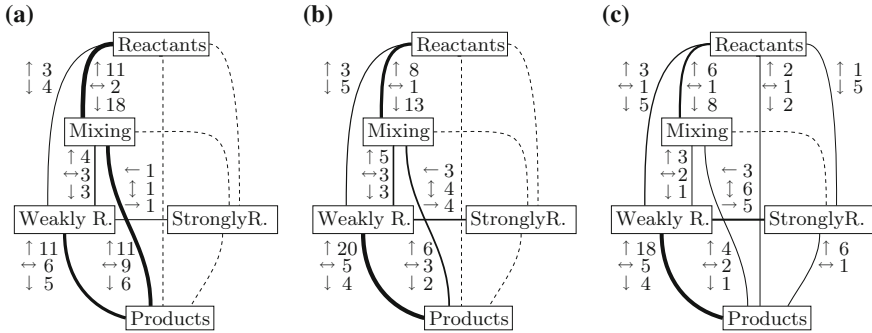


Fig. 6 Multi-fluid interface diagram for DME/air at $\Phi = 0.6$ and a supporting HCP temperature of: **a** $T_{HCP} = 1600$, **b** 1700 and **c** 1800 K. The weighted connections and values illustrate the number of interfaces in % and the arrows indicate the flow direction (\updownarrow with \leftrightarrow indicating near tangential flow). The total numbers of interfaces are 6700, 7900 and 7500 for $T_{HCP} = 1600$, 1700 and 1800 K

Unconditional velocity statistics were obtained 1 mm away from the upper nozzle exit, see Fig. 7a, and along the theoretical stagnation point streamline; see Fig. 7b. The former show nearly identical inlet velocity statistics for all T_{HCP} conditions. By contrast, with increasing T_{HCP} a modest reduction of the mean axial velocity along the stagnation point streamline is observed with a pronounced reduction in axial ($\sqrt{u'u'}/U_b$) and radial ($\sqrt{v'v'}/U_b$) velocity fluctuations. This can be attributed to the earlier onset of exothermic reactions and additional dilatation at higher temperature HCP blending and a resulting stronger impact on the flow field. Similar trends have been observed with increasing UN reactivity (i.e. Φ) by Goh et al. [20, 33] and Hamp and Lindstedt [22].

5.4 Conditional Velocity Statistics

Multi-fluid conditional velocity statistics [22] are used to clarify the influence of the HCP enthalpy as defined in Eq. 5.

$$\begin{aligned}
 \overline{U}_{k,FS,i,j} &= \frac{1}{N} \sum_{n=1}^N c_{FS,n,i,j} \cdot U_{k,n,i,j} \quad \forall i, j \\
 (u'u')_{k,FS,i,j} &= \frac{1}{N} \sum_{n=1}^N c_{FS,n,i,j} \cdot (U_{k,n,i,j} - \overline{U}_{k,FS,i,j})^2 \quad \forall i, j \\
 C_{FS,i,j} &= \frac{1}{N} \sum_{n=1}^N c_{FS,n,i,j} \quad \forall i, j
 \end{aligned} \tag{5}$$

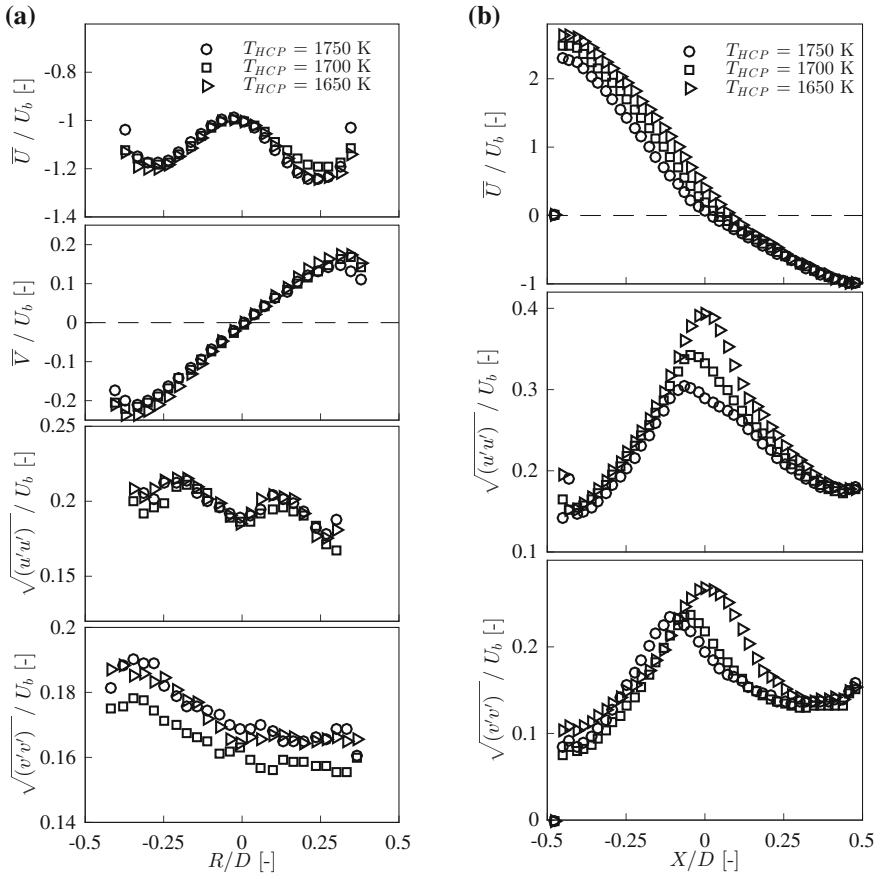


Fig. 7 Unconditional velocity statistics measured; **a** 1 mm of the UN exit: Mean axial velocity (top), mean radial velocity (2nd), axial velocity fluctuations (3rd) and radial velocity fluctuations (bottom) for varying HCP enthalpy; **b** along the stagnation point streamline for varying HCP enthalpy: Mean axial velocity (top row), axial velocity fluctuations (middle row) and radial velocity fluctuations (bottom row). Only every second data point is drawn to enhance the readability

In Eq. 5, $c_{FS,n}$ is the instantaneous (n) conditioning variable (i.e. unity within the individual fluid state (FS) and nil elsewhere), k the velocity component, N the total number of images (3000) and i and j the index variables. The sum of all fluid state progress variables (C_{FS}) is unity. The conditional velocity statistics were evaluated along the theoretical SPS and aligned at the instantaneous $x_s = 0$; see Fig. 3. A minimum of 75 vectors was used for the determination of conditional velocities. The conditional mean axial fluid state (FS) velocities ($\bar{U}_{0,FS}$) and axial ($\sqrt{u'u'_{0,FS}}$) and radial ($\sqrt{v'v'_{0,FS}}$) fluctuations were normalised by the respective reactant values measured 1 mm away from the upper nozzle exit; see Fig. 7a.

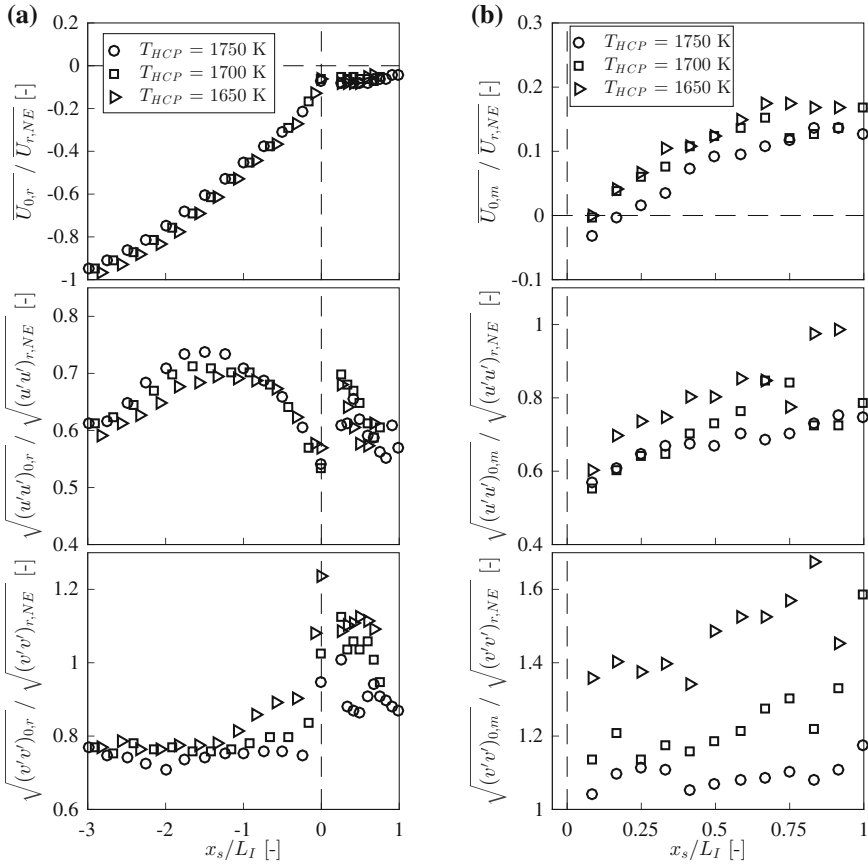


Fig. 8 Conditional mean axial **a** reactant and **b** mixing fluid velocity and fluctuations for varying HCP enthalpy along the stagnation point streamline aligned at the Mie scattering iso-contour ($x_s = 0$): Top— $\overline{U_{0,FS}}/\overline{U_{r,NE}}$; Middle— $\sqrt{(u'u')_{0,FS}}/\sqrt{(u'u')_{r,NE}}$; Bottom— $\sqrt{(v'v')_{0,FS}}/\sqrt{(v'v')_{r,NE}}$. At $x_s/L_I < 0$ only every third data point is plotted to enhance the readability. At $x_s/L_I > 0$, all data points are shown

5.4.1 Conditional Reactant Fluid Velocity

The conditional reactant fluid velocity is depicted in Fig. 8a. The reaction onset is anchored at a fixed mean reactant fluid velocity with $\overline{U_{0,r}} = -0.58 \pm 0.05 \text{ m s}^{-1}$ at $x_s = 0$. The axial velocity fluctuations are only just affected by the HCP enthalpy with the slight increase around $x_s/L_I \simeq -1.5$ consistent with modest differences in the mean velocity. The radial fluctuations show a tendency to increase close to the origin with decreasing T_{HCP} and a consistent increase in $\sqrt{v'v'_{0,R}}/\sqrt{v'v'_{r,NE}}$ is observed at $x_s > 0$. This can be attributed to a reaction onset that is increasingly governed by strong HCP blending.

5.4.2 Conditional Mixing Fluid Velocity

The impact of the HCP enthalpy on the thermally altered fluids is evident for the conditional mixing fluid velocity ($\overline{U_{0,m}/U_{r,NE}}$). The fluid pockets become increasingly driven by the HCP momentum for reduced T_{HCP} as shown in Fig. 8b. The value of $\overline{U_{0,m}/U_{r,NE}} < 0$ in the direct proximity of the origin (i.e. in line with the reactant flow) for $T_{HCP} = 1750$ K, while $\overline{U_{0,m}/U_{r,NE}} \geq 0$ for $T_{HCP} \leq 1700$ K. Moreover, with decreasing T_{HCP} the axial and radial velocity fluctuations increase. This is consistent with the theoretical discussion on increased auto-ignition delay times with decreasing T_{HCP} , see Fig. 2, and the need for additional HCP blending with reactants prior the onset of OH producing reactions. Similar trends for decreasing mixture reactivity have been observed by Hampp and Lindstedt [22].

5.4.3 Conditional Weakly Reacting Fluid Velocity

The weakly reacting fluid velocity $\overline{U_{0,w}/U_{r,NE}}$ is independent of the HCP enthalpy in the proximity of the origin as shown in Fig. 9a. The impact becomes increasingly evident for $x_s/L_I > 0.5$ leading to a separation of $\overline{U_{0,w}/U_{r,NE}}$. The reduced gradients with higher T_{HCP} are caused by the more distinct dilatation due to the reduced HCP blending fraction required to initiate combustion (e.g. OH producing reactions). The values of $\sqrt{(u'u')_{0,w}/(u'u')_{r,NE}}$ and $\sqrt{(v'v')_{0,w}/(v'v')_{r,NE}}$ show a modest reduction with increasing T_{HCP} that is consistent with the changes in the mixture reactivity [22]. The weakly reacting axial velocity fluctuations show a modest decrease ($\sim 10\%$) compared to the mixing fluid, while the radial component exhibits elevated ($\sim 10\%$) fluctuations. This can be attributed to the heat release associated with the OH producing chemical reactions and the corresponding modestly enhanced dilatation of the fluid state.

5.4.4 Conditional Strongly Reacting Fluid Velocity

The conditional mean axial strongly reacting fluid velocity is insensitive to the thermal support as depicted in Fig. 9b. This is characteristic for self-sustained burning at constant Da and Re_t in the absence (or with vanishing levels) of HCP dilution. In the direct proximity of the origin, the $\overline{U_{0,s}/U_{r,NE}}$ is consistently aligned with the reactant flow direction. Away from the origin, the strongly reacting fluid flow is increasingly governed by the momentum of the HCP stream, yet at significantly attenuated levels compared to the weakly reacting fluid. The axial ($\sqrt{(u'u')_{0,s}/(u'u')_{r,NE}}$) and radial ($\sqrt{(v'v')_{0,s}/(v'v')_{r,NE}}$) fluctuations show a distinct reduction with increasing HCP enthalpy that is more pronounced than the weakly reacting velocity fluctuations due to the impact of increased dilatation.

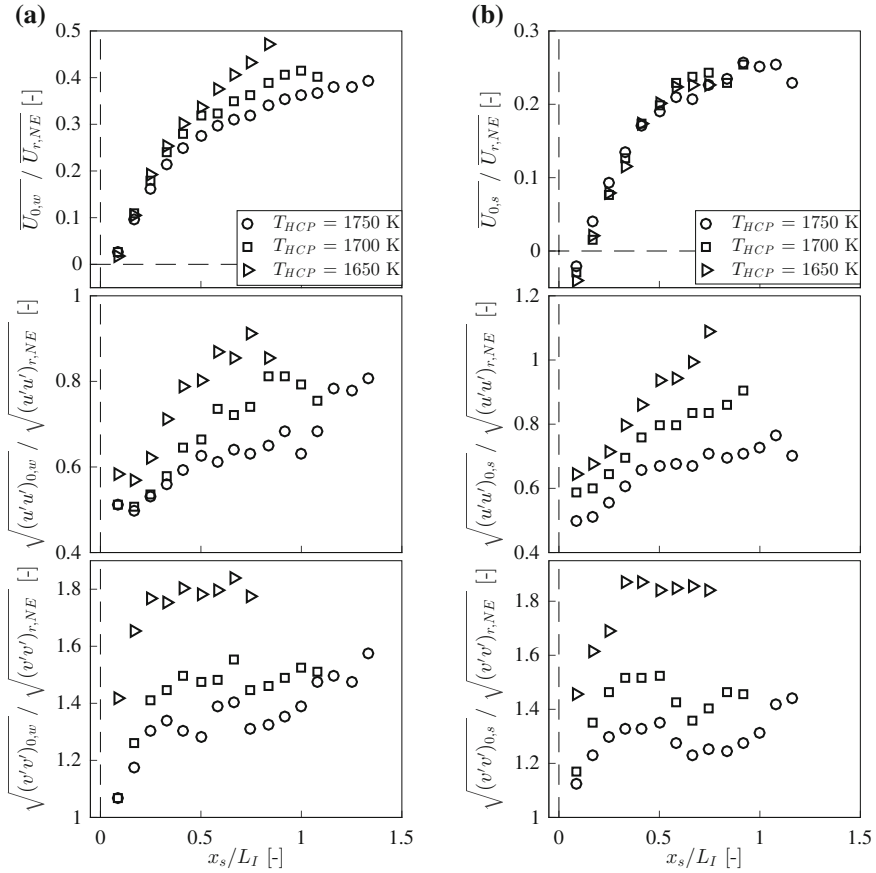


Fig. 9 Conditional mean axial **a** weakly and **b** strongly reacting fluid velocity and fluctuations for varying HCP enthalpy along the stagnation point streamline aligned at the Mie scattering iso-contour ($x_s = 0$): Top— $\overline{U_{0,FS}}/\overline{U_{r,NE}}$; Middle— $\sqrt{(u'u')_{0,FS}}/\sqrt{(u'u')_{r,NE}}$; Bottom— $\sqrt{(v'v')_{0,FS}}/\sqrt{(v'v')_{r,NE}}$

5.5 Conditional Strain on Material Surfaces

The in-plane velocity gradients were conditioned upon the fluid state material surfaces (β) [23]. The strain rate ($e_{ij} = 0.5(\partial u_i/\partial x_j + \partial u_j/\partial x_i)$) and vorticity ($\omega_{ij} = \partial u_i/\partial x_j - \partial u_j/\partial x_i$) were determined from the instantaneous planar PIV data and subsequently conditioned upon β . The normal (a_n), tangential (a_t) and total ($a_d = e_{\beta,11} + e_{\beta,22}$) strain as well as vorticity were determined for the cases $T_{HCP} = 1650, 1700$ and 1750 K within $\pm L_I/2$ radially away from the theoretical SPS to include the movement of the stagnation point [32].

Table 4 Mean and spread of the PDFs of the normal (a_n), tangential (a_t) and total (a_d) strain and vorticity (ω) conditioned upon the fluid state iso-contours (β) for $T_{HCP} = 1650, 1700$ and 1750 K. R—reactants; M—mixing; WR—weakly reacting; SR—strongly reacting; P—product fluid

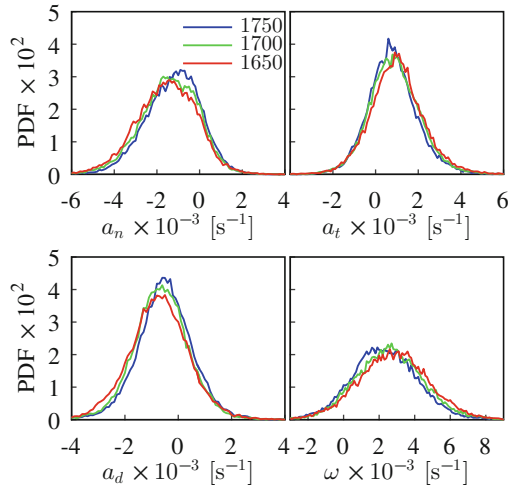
T_{HCP}	β	Mean				Spread (rms)			
		a_n	a_t	a_d	ω	a_n	a_t	a_d	ω
1750 K	R	-1251	802	-504	2312	886	760	737	1351
1700 K	R	-1414	890	-643	2578	924	801	727	1391
1650 K	R	-1569	996	-733	2813	964	829	808	1442
1750 K	M	-1350	699	-401	2383	1060	763	826	1533
1700 K	M	-1611	767	-614	2758	1102	822	811	1581
1650 K	M	-1827	912	-735	3099	1177	897	925	1669
1750 K	WR	-1248	709	-521	2378	872	734	762	1331
1700 K	WR	-1450	737	-797	2690	928	858	786	1413
1650 K	WR	-1534	915	-717	2948	987	888	876	1512
1750 K	SR	-920	660	-276	1953	806	729	743	1278
1700 K	SR	-1138	668	-544	2296	861	810	767	1353
1650 K	SR	-1248	778	-479	2575	956	929	901	1522
1750 K	P	-1477	821	-518	2682	991	791	801	1452
1700 K	P	-1801	882	-889	3127	1029	870	815	1501
1650 K	P	-1915	1052	-849	3429	1125	923	901	1625

5.5.1 Strain Distribution on the Reactant Fluid Surface

The normal (a_n) and tangential (a_t) strain conditioned upon the reactant fluid iso-contour (R) are depicted in Fig. 10 along with the corresponding total rate of strain (a_d) and vorticity (ω). To recapitulate, the HCP from the LN exerted a vanishing effect on the conditional reactant fluid velocities. The $a_n|R$, however, shows a modest shift of the PDF towards reduced mean compressive values ($-1570 < a_n \text{ (s}^{-1}\text{)} < -1250$ for $1650 < T_{HCP}\text{(K)} < 1750$). The reduction can be attributed to increased flow acceleration of adjacent reactive fluid states and slight detachment of the reactant fluid iso-contour from the stagnation plane [23]. The latter further yields a reduced mean tangential ($1000 < a_t \text{ (s}^{-1}\text{)} < 800$) and total contracting ($-730 < a_d \text{ (s}^{-1}\text{)} < -500$) strain with reduced mean vorticity levels ($2810 < \omega \text{ (s}^{-1}\text{)} < 2310$). Moreover, the spread of all PDFs is reduced by $\sim 10\%$ with increasing T_{HCP} . This suggests a first thermal alteration that is increasingly caused by adjacent exothermic reactions with a distinct dilatation direction that is consistent with the observed interface statistics in Sect. 5.2 and the study presented by Hampf and Lindstedt [23].

The velocity gradients conditioned upon the mixing ($a_n|M$, $a_t|M$, $\omega|M$) and weakly reacting fluid surfaces ($a_n|WR$, $a_t|WR$, $\omega|WR$) exhibit similar trends to the reactant fluid and are thus not discussed separately. Values are listed in Table 4.

Fig. 10 PDF of the rate of strain and vorticity evaluated along the reactant fluid iso-contour: Top left: Normal strain; Right: Tangential strain; Bottom left: Total strain; Right: Vorticity. The legend entries refer to T_{HCP} [K]



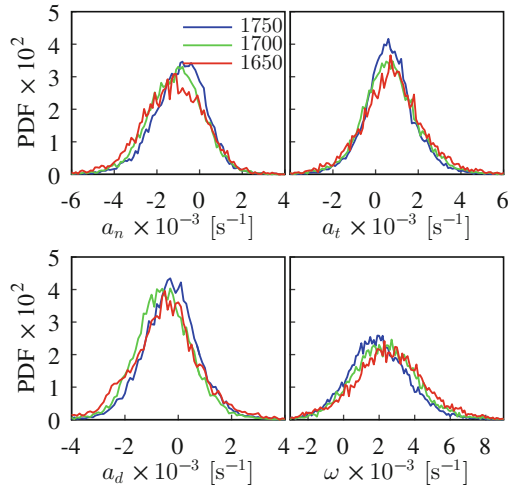
5.5.2 Strain Distribution on the Strongly Reacting Fluid Surface

The rate of strain and vorticity conditioned upon the strongly reacting (SR) fluid material surface ($a_n|SR$, $a_t|SR$, $a_d|SR$, $\omega|SR$) are depicted in Fig. 11. For $T_{HCP} = 1750$ K, the reaction onset is anchored in comparatively low compressive strain regions with a mean of $a_n = -920$ s^{-1} in contrast with -1250 s^{-1} for $T_{HCP} = 1650$ K. The normal strain along the strongly reacting fluid material surface is $\sim 30\%$ lower than the rate of strain on the reactant and weakly reacting fluid iso-contour. The $PDF(a_n|SR)$ at $T_{HCP} = 1750$ K further shows an elevated skewness towards decreased compressive strain compared to lower HCP temperature as well as to fluid states with reduced reactivity. The merging of the strongly reacting material surface with the stagnation plane with decreasing T_{HCP} results in higher tangential strain ($660 < a_t$ (s^{-1}) < 780) as well as a_d . The corresponding Euclidean norm, defined in Eq. 6, increases from $1132 < |a_{SR}|$ (s^{-1}) < 1471 with decreasing T_{HCP} .

$$|a_{SR}| = \sqrt{a_{n|SR}^2 + a_{t|SR}^2} \quad (6)$$

The extinction strain of the corresponding laminar flame was determined to $a_q = 600$ s^{-1} [22]. The increasing ratio from $0.41 < a_q/|a_{SR}| < 0.53$ with T_{HCP} further highlights the enhanced likelihood of establishing a self-sustained flame. The elevated skewness and reduced spread of the $PDF(a_n)$ and $PDF(a_t)$ with increasing reactivity was also observed by Hampp and Lindstedt [23] and Hartung et al. [49]. The lack of a preferential alignment of the flame normal with the extensive rate of strain at modest dilatation was also discussed by Chakraborty and Swaminathan [50]. A change of T_{HCP} from 1650 to 1750 K causes a 25% vorticity reduction, and the

Fig. 11 PDF of the rate of strain and vorticity evaluated along the strongly reacting fluid iso-contour: Top left: Normal strain; Right: Tangential strain; Bottom left: Total strain; Right: Vorticity. The legend entries refer to T_{HCP} [K]

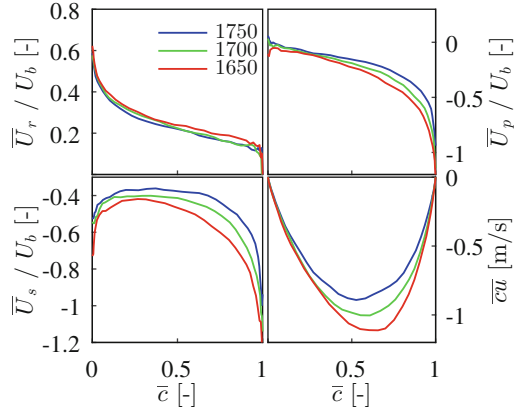


values are up to 15% lower than for the reactant or weakly reacting fluid material surface (see Table 4).

5.6 Bimodal Flow Analysis

Bimodal statistics [29] were obtained by combining the thermally altered fluid states (i.e. mixing, weakly reacting, strongly reacting and product fluid) as products, defining the reaction progress variable (\bar{c}) [23, 29]. This illustrates the impact of the HCP enthalpy on the turbulent flame brush and scalar transport. The reactant fluid velocity (\bar{U}_r/U_b) is only marginally affected by the HCP temperature (see Fig. 12). The observation is consistent with the multi-fluid analysis, which showed that reactant fluid statistics are independent of the HCP enthalpy (see Figs. 4 and 8a–9b). By contrast, the velocity of the combined product fluid (\bar{U}_p/U_b) shows a distinct impact of the HCP support on the flame brush for $\bar{c} > 0.25$ as increasing amounts of HCP are required to sustain chemical activity with decreasing T_{HCP} . This results in \bar{U}_p/U_b being increasingly governed by the HCP stream momentum. By contrast, higher T_{HCP} values necessitate reduced HCP blending fractions, result in a more pronounced dilatation and, in turn, reduced slip velocities (\bar{U}_s/U_b). The increased dilatation further yields a noticeable reduction in the gradient scalar flux ($\bar{c}u$) as also shown in Fig. 12. However, a transition to counter-gradient transport is not observed. A similar impact on scalar transport was also observed by Goh et al. [18, 20] and Hampf and Lindstedt [23].

Fig. 12 Mean conditional reactant (\bar{U}_r , top left) and product (\bar{U}_p , top right) velocities in progress variable (\bar{c}) space along with the slip velocity (\bar{U}_s , bottom left) and scalar flux ($\bar{c}\bar{u}$, bottom right) for varying HCP enthalpy. The legend entries refer to T_{HCP} [K]



6 Conclusions

The impact of the burnt gas state on the combustion of lean premixed DME/air flames in fractal grid generated multi-scale turbulence with constant $\Phi = 0.6$, $Re_t \simeq 395$, $Da \simeq 1.1$ and $Ka \simeq 7.0$ was investigated. The temperature of the hot combustion products, emerging the lower nozzle of a back-to-burnt opposed jet configuration, was varied ($1600 < T_{HCP}(\text{K}) < 1800$) by means of the CO_2 dilution level. The variation ranges from close to the extinction temperature ($T_q \simeq 1570$ K) of the corresponding twin flame configuration to beyond the unstrained adiabatic flame temperature ($T_{ad} \simeq 1750$ K). The burning mode transition was quantified by means of a multi-fluid analysis. With increasing T_{HCP} , combustion shifts progressively away from strong HCP dilution influence towards self-sustained burning that may be initialised by small HCP blending fractions or contact burning. By contrast, the strongly reacting fluid (representing self-sustained burning) nearly vanished for T_{HCP} of the order of the extinction temperature. The impact of turbulence–chemistry interaction on the flow field was evaluated in the range $1650 < T_{HCP}(\text{K}) < 1750$. With increasing HCP enthalpy a gradually stronger and more directed dilatation was observed that caused a reduction in the gradient scalar flux. Characteristic for self-sustained burning and the velocity statistics of the strongly reacting fluid were not affected by the HCP enthalpy. However, the strain distribution along the material surfaces indicated a gradual detachment of the reaction onset from the stagnation plane and adjacent flow acceleration with increasing T_{HCP} . By contrast, at reduced T_{HCP} the chemically active fluids were governed by the thermal support and characterised by high vorticity and rates of strain. The current data set is expected to challenge numerical models that aim to delineate combustion mode transitions.

Acknowledgements The authors would like to acknowledge the support of the AFOSR and EOARD under Grant FA9550-17-1-0021 and thank Dr. Chiping Li and Dr. Russ Cummings for encouraging the work. The US Government is authorised to reproduce and distribute reprints for

Governmental purpose notwithstanding any copyright notation thereon. The authors would also like to thank Dr. Robert Barlow for his support.

References

1. F.J. Weinberg, Combustion temperatures: the future? *Nature* **233**, 39–241 (1971)
2. E. Mastorakos, A.M.K.P. Taylor, J.H. Whitelaw, Extinction of turbulent counterflow flames with reactants diluted by hot products. *Combust. Flame* **102**, 101–114 (1995)
3. J.A. Wünnig, J.G. Wünnig, Flameless oxidation to reduce thermal NO-formation. *Prog. Energy Combust.* **23**, 81–94 (1997)
4. I.B. Özdemir, N. Peters, Characteristics of the reaction zone in a combustor operating at mild combustion. *Exp. Fluids* **30**, 683–695 (2001)
5. Z. Zhao, A. Kazakov, J. Li, F.L. Dryer, The initial temperature and N₂ dilution effect on the laminar flame speed of propane/air. *Combust. Sci. Technol.* **176**, 1705–1723 (2004)
6. H.J. Curran, S.L. Fischer, F.L. Dryer, Reaction kinetics of dimethylether. II: Low-temperature oxidation in flow reactors. *Int. J. Chem. Kinet.* **32**, 741–759 (2000)
7. R. Lückerrath, W. Meier, M. Aigner, FLOX combustion at high pressure with different fuel compositions. *J. Eng. Gas Turb. Power* **130**, 011505 (2008)
8. T. Plessing, N. Peters, J.G. Wünnig, Laseroptical investigation of highly preheated combustion with strong exhaust gas recirculation. *Proc. Combust. Inst.* **27**, 3197–3204 (1998)
9. J. Sidey, E. Mastorakos, R.L. Gordon, Simulations of autoignition and laminar premixed flames in methane/air mixtures diluted with hot products. *Combust. Sci. Technol.* **186**, 453–465 (2014)
10. Y. Minamoto, N. Swaminathan, R.S. Cant, T. Leung, Reaction zones and their structure in MILD combustion. *Combust. Sci. Technol.* **186**, 1075–1096 (2014)
11. B. Zhou, C. Brackmann, Q. Li, Z. Wang, P. Petersson, Z. Li, M. Aldén, X.-S. Bai, Distributed reactions in highly turbulent premixed methane/air flames. Part I. Flame structure characterization. *Combust. Flame* **162**, 2937–2953 (2015)
12. B. Zhou, C. Brackmann, Z. Li, M. Aldén, X.-S. Bai, Simultaneous multi-species and temperature visualization of premixed flames in the distributed reaction zone regime. *Proc. Combust. Inst.* **35**, 1409–1416 (2015)
13. B. Zhou, C. Brackmann, Z. Wang, Z. Li, M. Richter, M. Aldén, X.-S. Bai, Thin reaction zone and distributed reaction zone regimes in turbulent premixed methane/air flames: scalar distributions and correlations. *Combust. Flame* **175**, 220–236 (2016)
14. A.R. Masri, R.W. Dibble, R.S. Barlow, The structure of turbulent nonpremixed flames revealed by Raman-Rayleigh-LIF measurements. *Prog. Energy Combust. Sci.* **22**, 307–362 (1996)
15. R.S. Barlow, J.H. Frank, Effects of turbulence on species mass fractions in methane/air jet flames. *Proc. Comb. Inst.* **27**, 1087–1095 (1998)
16. D. Geyer, A. Kempf, A. Dreizler, J. Janicka, Turbulent opposed-jet flames: a critical benchmark experiment for combustion LES. *Combust. Flame* **143**, 524–548 (2005)
17. K.H.H. Goh, P. Geipel, R.P. Lindstedt, Lean premixed opposed jet flames in fractal grid generated multiscale turbulence. *Combust. Flame* **161**, 2419–2434 (2014)
18. Goh KHH (2013) Investigation of conditional statistics in premixed combustion and the transition to flameless oxidation in turbulent opposed jets. Ph.D. thesis, Imperial College. <http://hdl.handle.net/10044/1/28073>
19. B. Coriton, J.H. Frank, A. Gomez, Effects of strain rate, turbulence, reactant stoichiometry and heat losses on the interaction of turbulent premixed flames with stoichiometric counterflowing combustion products. *Combust. Flame* **160**, 2442–2456 (2013)
20. K.H.H. Goh, P. Geipel, F. Hampf, R.P. Lindstedt, Regime transition from premixed to flameless oxidation in turbulent JP-10 flames. *Proc. Combust. Inst.* **34**, 3311–3318 (2013)
21. K.H.H. Goh, P. Geipel, R.P. Lindstedt, Turbulent transport in premixed flames approaching extinction. *Proc. Combust. Inst.* **35**, 1469–1476 (2015)

22. F. Hampp, R.P. Lindstedt, Quantification of combustion regime transitions in premixed turbulent DME flames. *Combust. Flame* **182**, 248–268 (2017)
23. F. Hampp, R.P. Lindstedt, Strain distribution on material surfaces during combustion regime transitions. *Proc. Combust. Inst.* **36**, 1911–1918 (2017)
24. B. Coriton, M.D. Smooke, A. Gomez, Effect of the composition of the hot product stream in the quasi-steady extinction of strained premixed flames. *Combust. Flame* **157**, 2155–2164 (2000)
25. E. Abtahizadeh, J. van Oijen, P. de Goeij, Numerical study of mild combustion with entrainment of burned gas into oxidizer and/or fuel streams. *Combust. Flame* **159**, 2155–2165 (2012)
26. T. Fleisch, C. McCarthy, A. Basu, C. Udovich, P. Charbonneau, W. Slodowske, S.-E. Mikkelsen, J. McCandless, A new clean diesel technology: demonstration of ULEV emissions on a Navistar diesel engine fueled with dimethyl ether, SAE, 950061 (1995)
27. S.C. Sorenson, S.E. Mikkelsen, Performance and emissions of a 0.273 liter direct injection diesel engine fuelled with neat dimethyl ether, SAE, 950064 (1995)
28. S.-W. Park, Detailed chemical kinetic model for oxygenated fuels. Ph.D. thesis, Imperial College. <http://hdl.handle.net/10044/1/9599> (2012)
29. K.N.C. Bray, Laminar flamelets and the Bray, Moss, and Libby Model, in *Turbulent Premixed Flames*, ed. by N. Swaminathan, K.N.C. Bray (Cambridge University Press, 2001), pp. 41–60. ISBN: 978-0-521-76961-7
30. F. Hampp, Quantification of combustion regime transitions. Ph.D. thesis, Imperial College. <http://hdl.handle.net/10044/1/32582> (2016)
31. F. Hampp, R.P. Lindstedt, Fractal grid generated turbulence—a bridge to practical combustion applications, in *Fractal Flow Design: How to Design Bespoke Turbulence and Why*. CISM International Centre for Mechanical Sciences 568, ed. by Y. Sakai, C. Vassilicos (Springer, 2016). https://doi.org/10.1007/978-3-319-33310-6_3
32. P. Geipel, K.H.H. Goh, R.P. Lindstedt, Fractal-generated turbulence in opposed jet flows. *Flow Turbul. Combust.* **85**, 397–419 (2010)
33. K.H.H. Goh, P. Geipel, F. Hampp, R.P. Lindstedt, Flames in fractal grid generated turbulence. *Fluid Dyn. Res.* **45**, 061403 (2013)
34. N. Peters, Kinetic foundation of thermal flame theory, in *Advances in Combustion Science: In Honor of Y. B. Zel'dovich*. Progress in Astronautics and Aeronautics 173, ed. by W.A. Sirignano, A.G. Merzhanov, L. de Luca (AIAA, 1997), pp. 73–91
35. J. Kerl, T. Sponfeldner, F. Beyrau, An external Raman laser for combustion diagnostics. *Combust. Flame* **158**, 1905–1907 (2011)
36. B. Wieneke, K. Pfeiffer, Adaptive PIV with variable interrogation window size and shape, in *15th International Symposium on the Application of Laser Techniques to Fluid Mechanics* (2010). http://tces.dem.ist.utl.pt/LXLASER/lxaser2010/upload/1845_qkuqls_1.12.3.Full_1845.pdf
37. W.P. Jones, R.P. Lindstedt, The calculation of the structure of laminar counterflow diffusion flames using a global reaction mechanism. *Combust. Sci. Technol.* **61**, 31–49 (1988)
38. J. Sidey, E. Mastorakos, Visualization of MILD combustion from jets in cross-flow. *Proc. Combust. Inst.* **35**, 3537–3545 (2015)
39. Y. Minamoto, N. Swaminathan, Scalar gradient behaviour in MILD combustion. *Combust. Flame* **161**, 1063–1075 (2014)
40. Y. Minamoto, N. Swaminathan, S.R. Cant, T. Leung, Morphological and statistical features of reaction zones in MILD and premixed combustion. *Combust. Flame* **161**, 2801–2814 (2014)
41. W.K. George, H.J. Hussein, Locally axisymmetric turbulence. *J. Fluid Mech.* **233**, 1–23 (1991)
42. I.G. Shepherd, R.K. Cheng, P.J. Goix, The spatial scalar structure of premixed turbulent stagnation point flames. *Proc. Combust. Inst.* **23**, 781–787 (1991)
43. A.M. Steinberg, J.F. Driscoll, S.L. Ceccio, Measurements of turbulent premixed flame dynamics using cinema stereoscopic PIV. *Exp. Fluids* **44**, 985–999 (2008)
44. B. Böhm, C. Heeger, I. Boxx, W. Meier, A. Dreizler, Time-resolved conditional flow field statistics in extinguishing turbulent opposed jet flames using simultaneous highspeed PIV/OH-PLIF. *Proc. Combust. Inst.* **32**, 1647–1654 (2009)

45. B.E. Battles, R.K. Hanson, Laser-induced fluorescence measurements of NO and OH mole fraction in fuel-lean, high-pressure (1–10 atm) methane flames: fluorescence modeling and experimental validation. *J. Quant. Spectrosc. Radiat. Transf.* **54**, 521–537 (1995)
46. S. Krishna, R.V. Ravikrishna, Quantitative OH planar laser induced fluorescence diagnostics of syngas and methane combustion in a cavity combustor. *Combust. Sci. Technol.* **187**, 1661–1682 (2015)
47. K.A. Buch, W.J.A. Dahm, Experimental study of the fine-scale structure of conserved scalar mixing in turbulent shear flows. Part 2. $Sc = 1$. *J. Fluid Mech.* **364**, 1–29 (1998)
48. G.K. Batchelor, Small-scale variation of convected quantities like temperature in turbulent fluid. Part 1. General discussion and the case of small conductivity. *J. Fluid Mech.* **5**, 113–133 (1959)
49. G. Hartung, J. Hult, C.F. Kaminski, J.W. Rogerson, N. Swaminathan, Effect of heat release on turbulence and scalar-turbulence interaction in premixed combustion. *Phys. Fluids* **20**, 035110 (2008)
50. N. Chakraborty, N. Swaminathan, Influence of the Damköhler number on turbulence-scalar interaction in premixed flames. I. Physical insight. *Phys. Fluids* **19**, 045103 (2007)